

Revisiting Energy Distribution and Formation Rate of CHIME Fast Radio Bursts

K. J. Zhang¹, X. F. Dong^{2,3}, A. E. Rodin⁴, V. A. Fedorova⁴, Y. F. Huang³, D. Li⁵, P. Wang⁵, Q. M. Li¹, C. Du³, F. Xu³,
and Z. B. Zhang^{1,*}

¹ Department of Physics, Guizhou University, Guiyang 550025, P. R. China. e-mail: z-b-zhang@163.com

² School of Physics and Physical Engineering, Qufu Normal University, Qufu 273165, P. R. China

³ School of Astronomy and Space Science, Nanjing University, Nanjing 210023, P. R. China

⁴ P. N. Lebedev Physical Institute of the Russian Academy of Sciences, Leninsky prospekt, 53, Moscow, 119991, Russia

⁵ National Astronomical Observatories, Chinese Academy of Sciences, Beijing 100101, P. R. China

Received; accepted:

ABSTRACT

Using a large sample of fast radio bursts (FRBs) from the first CHIME/FRB catalog, we apply the Lynden-Bell's c^- method to study their energy function and formation rate evolutions with redshift. It is found with the non-parametric Kendall's τ statistics that the FRB energy strongly evolves with the cosmological redshift as $E(z) \propto (1+z)^{5.23}$. After removing the redshift dependence, the local energy distribution can be described by a broken power-law form of $\Psi(E_0) \propto E_0^{-0.38}$ for the low-energy segment and $\Psi(E_0) \propto E_0^{-2.01}$ for the high-energy segment with a dividing line of $\sim 2.1 \times 10^{40}$ erg. Interestingly, we find that the formation rate of CHIME FRBs also evolves with redshift as $\rho(z) \propto (1+z)^{-4.73 \pm 0.08}$. The local formation rate $\rho(0)$ of the CHIME FRBs is constrained to be about $1.25 \times 10^4 \text{ Gpc}^{-3} \text{ yr}^{-1}$ that is comparable with some previous estimations. In addition, we notice the formation rate not only exceeds the star formation rate at the lower redshifts but also always declines with the increase of redshift, which does not match the star formation history at all. Consequently, we suggest that most FRBs could originate from the older stellar populations.

Key words. Stars: formation-Stars: late-type-Stars: energy function-Radio continuum: general-methods: data analysis

1. INTRODUCTION

Over the past decade, Fast radio bursts (FRBs) have motivated more and more people's research interests in seeking for their physical origins. Unfortunately, the progenitors and central engines of FRBs are still unclear in nature. Many authors proposed that they may associate with star formation regions inside galaxies and can be explained by different progenitors such as black holes (BHs), magnetars, supernovae (SNe), neutron stars (NSs), etc. (e.g. Platts et al. 2019; Zhang 2020; Xiao et al. 2021; Petroff et al. 2022)¹. Accurate localization of FRBs in their host galaxies can offer good clue to their origins. The host galaxies of roughly two dozen FRBs have been successfully identified² (Heintz et al. 2020, reference therein). For instance, the detection of a bright FRB 20200428 originating from the galactic magnetar SGR 1935+2154 provides an important link between FRBs and magnetars (CHIME/FRB Collaboration et al. 2020; Bochenek et al. 2020; Lin et al. 2020; Mereghetti et al. 2020; Li et al. 2021a; Ridnaia et al. 2021; Tavani et al. 2021; Wada & Ioka 2023). Thus, the magnetar model is one of the most likely explanations for FRBs as the magnetar-based models can reproduce multiple FRB characteristics (Zhang 2020). Importantly, magnetars can be formed in both young (via core-collapse SNe) and old (namely white dwarf (WD) -NS coalescence, accretion induced collapse (AIC) and other compact binary coalescences) star populations.

Good localization can also help identify FRB progenitors according to distinct galactic environments (Kremer et al. 2021; Popov S. & Pshirkov M. 2023). It was found that most well-localized FRBs such as FRB 20121102A (Tendulkar et al. 2017), FRB 20190520B (Niu et al. 2022) and FRB 20190303A (Michilli et al. 2023) are generally generated from active or quasi star-forming galaxies (e.g., Tendulkar et al. 2017; Bannister et al. 2019; Prochaska et al. 2019; Marcote et al. 2020; Fong et al. 2021; Ravi et al. 2022; Niu et al. 2022; Bhandari et al. 2023; Law et al. 2023; Gordon et al. 2023). In this situation, it will be expected that young star populations should be favored as the origin of FRBs. However, there are some well-localized FRBs whose host galaxies are quiescent instead of star-forming. For example, the optical observations reveal that FRB 20201124A was situated in an inter-arm region of a barred-spiral galaxy, in which the galactic environment does not comply with the young star populations (Xu et al. 2021). In addition, FRB 20220509G is recorded to localize in a quiescent galaxy (Law et al. 2023). Furthermore, the host galaxy location of FRB 20180916B was found to deviate from the star-forming region (Tendulkar et al. 2021). Therefore, the explanation of this phenomenon is that at least some FRBs are associated with old star populations, namely NSs and BHs (see, e.g., Mottez & Zarka 2014; Zhang 2017; Deng et al. 2018; Zhang & Zhang 2022). In particular, FRB 20200120E is identified to be within an old globular cluster with an age of 9 Gyr in the extragalaxy M81 (Bhardwaj et al. 2021; Kirsten et al. 2022). As a whole, FRB host galaxies have two kinds of environments, that is the star formation region (e.g., Tendulkar et al. 2017; Bassa et al. 2017; Bannister et al. 2019;

¹ See <https://frbtheorycat.org>

² See <https://github.com/FRBs/FRBhostpage>

Tendulkar et al. 2021; Niu et al. 2022) and the star quiescent region (eg., Bhardwaj et al. 2021; Kirsten et al. 2022). It shows that FRBs might originate from multiple galactic environment channels. However, a very limited number of well-localized FRBs is inadequate to reveal the FRB origins.

With the increase of FRB numbers, a statistical study of luminosity/energy distributions is an alternative solution to disclose their progenitors. In other words, the luminosity/energy evolution with redshift or the formation rate (or co-moving density) evolution, is found to be an effective way to constrain the FRB origin models (e.g., Locatelli et al. 2019; Hashimoto et al. 2020a; Arcus et al. 2021; James et al. 2022; Zhang & Zhang 2022). Although the underlying physics of the FRBs still remains uncertain, the total energy output should be linked to the FRB progenitors. On the other hand, the progenitors of some FRBs are found to connect with the star-forming activity, which motivates us explore the FRB origins by describing how the luminosity/energy function and formation rate evolve with redshift. By contrast, the isotropic energy is reliably measured and the luminosity is usually uncertain since the intrinsic pulse width of most FRBs is unknown (Macquart & Ekers 2018; Ravi 2019; Pleunis et al. 2021a). Consequently, we analyze the energies instead of luminosities of FRBs in this work. The FRB energy function and their redshift evolution may provide an even more representative clue to constrain the possible FRB progenitors. Recently, Hashimoto et al. (2022) found that if FRBs are resulted from younger star populations tracking the cosmic star formation history, the FRB formation rate should increase with increasing redshift up to $z \sim 2$. They also speculated that the FRB formation rate may decrease towards higher redshifts if the origin of FRBs is related to old populations. This will help us constrain the progenitor models, plan the most adequate follow-up observations, and provide further clues to elucidate the origin of FRBs.

To estimate the formation rate of FRBs, several statistical methods such as the parametric methods including the direct fitting technique, the bayesian statistics (eg., Luo et al. 2018, 2020; Tang et al. 2023), the likelihood estimation (Marshall et al. 1983) and the non-parametric methods such as the V_{max} method (Hashimoto et al. 2020a,b, 2022), the V/V_{max} method (Locatelli et al. 2019) and the popular Lynden-Bell's c^- method, (e.g., Efron & Petrosian 1998; Petrosian et al. 2015; Yu et al. 2015; Deng et al. 2019; Dong et al. 2022) have been applied in the past (see also Dong et al. (2023) for a short review). For the purpose, the isotropic energy E or luminosity L is usually used to plot against the redshift z , where E or L shows an evolution with z for FRBs (Locatelli et al. 2019; Hashimoto et al. 2020a; James et al. 2022). However, this may be caused by the effect of instrument threshold truncation (see however Dong et al. 2022). Thus, as suggested by Deng et al. (2019) and Zhang & Zhang (2022), any attempt to measure the $E - z$ or $L - z$ correlation should carefully account for instrumental effect in advance. To mitigate instrumental selection effects between different telescopes, it is a typical practice to use a large and homogeneous sample collected by a single telescope. We here use the Kendall's τ statistics proposed by Efron & Petrosian (1992, 1998) to examine the correlation between energy and redshift. Then, we apply the Lynden-Bell's c^- methods to obtain the distributions of energy de-evolved with redshift and the formation rate history.

This paper is organized as follows. Section 2 describes the data reduction process. Section 3 presents the Lynden-Bell's c^- method and the non-parametric Kendall's τ statistics. In Section 4 we derive the FRB energy function in Section 4. The redshift distribution and formation rate are shown in Section 5. In Section 6, we give the local event rate of the sample

of CHIME FRBs. Finally, we end with conclusion and discussions in Section 7. Throughout the paper, a flat Λ CDM universe with $H_0 = 67.74 \text{ km s}^{-1} \text{ Mpc}^{-1}$, $\Omega_\Lambda = 0.6911$ and $\Omega_m = 0.3089$ (Planck Collaboration et al. 2016) is assumed.

2. SAMPLE SELECTION

Until March 2022, more than 700 FRBs had been observed³ (Spanakis-Misirlis 2021). Notably, the CHIME/FRB Collaboration published their first catalog of 482 FRBs of which 474 non-repeaters and 18 repeaters were involved. To weaken the selection bias effect, we select the FRB data detected by the CHIME telescope only⁴ as listed in Table A.1 (refer to CHIME/FRB Collaboration et al. 2021), where the selection criteria are (1) FRBs with $\text{bonsai_snr} < 10$ are rejected, (2) FRBs with fluence detected directly after a system restarts are chosen, (3) three FRBs (FRB20190210D, FRB20190125B, FRB20190202B) detected in far side-lobes were excluded, (4) FRBs detected during pre-commissioning, periods of low sensitivity or on days of software upgrades are excluded, (5) the first burst is taken if a FRB is repeating. Thus a sample of 396 CHIME FRBs have been chosen for this study. Phenomenologically, FRBs can be classified into repeaters and apparent non-repeaters. However, there are some FRBs classified as "one-off FRBs" that are actually repeating ones (eg., Kumar et al. 2019; Chen et al. 2022). Interestingly, Li et al. (2021b) proposed that FRBs are better to be classified into long and short groups on basis of the time durations. It is still unknown whether different kinds of FRBs have the same origin (eg., Caleb et al. 2019; Geng et al. 2021; Kirsten et al. 2023; Gordon et al. 2023). Unfortunately, there is a repeating FRB 20151125 exhibiting wider radio pulses detected by the Big Scanning Array of the Lebedev Physical Institute (BSA/LPI) (Fedorova, V. A., & Rodin, A. E. 2019b, ARep, 63, 877). Categorizing FRBs into repeaters and non-repeaters may be not intrinsic but surficial owing to the sensitivity limits or the observational time coverage (Ai et al. 2021), which motivates us to combine the repeating and non-repeating CHIME FRBs into a large sample uniformly.

Following Zhang (2018), we estimate the redshift of a FRB by its **extragalactic dispersion measure** (DM_E) as $z \sim DM_E/[855 \text{ pc cm}^3]$ and then calculate the isotropic energy at a central frequency of ν_c . Owing to the effects of frequency drift and cosmological time dialation, the observed FRB spectra should be corrected to the rest-frame in order to infer the detection rate accurately. The isotropic energy of a FRB is determined by

$$E = 4\pi D_L^2(z) F_{\text{obs}} \nu_c k(z) / (1+z), \quad (1)$$

where $D_L = c(1+z) \int_0^z 1/\{H_0 [(1+z)^3 \Omega_m + \Omega_\Lambda]^{1/2}\} dz$ is the luminosity distance, $\nu_c = 600 \text{ MHz}$ (Bandura et al. 2014; CHIME/FRB Collaboration et al. 2018, 2021) and $k(z)$ denote the central frequency and the K-correction factor, respectively. Assuming a power-law spectrum of $F \propto \nu^{-\beta}$ within a narrow radio band, we have calculated the parameter $k(z)$ defined by Lorimer et al. (2013); Cao et al. (2017); Zhang & Wang (2019); Bhattacharya & Kumar (2020) as

$$k(z) = \frac{\nu_{\text{max}}^{1-\beta} - \nu_{\text{min}}^{1-\beta}}{[(1+z)\nu_2]^{1-\beta} - [(1+z)\nu_1]^{1-\beta}}, \quad (2)$$

³ For a complete list of known FRBs, see <https://www.herta-experiment.org/frbstats> or the Transient Name Server (TNS, Petroff & Yaron 2020)

⁴ <https://www.chime-frb.ca/catalog>

where ν_{\min} and ν_{\max} are respectively the minimum and maximum frequencies of all FRBs in the rest frame. Here $\nu_{\min} = 100$ MHz and $\nu_{\max} = 8$ GHz have been assumed similar to some previous groups (Gajjar et al. 2018; Pastor-Marazuela et al. 2021; Pleunis et al. 2021b). β is the spectral index in radio band. ν_1 and ν_2 denote the observed frequency bands of CHIME, say, $\nu_1 = 400$ MHz and $\nu_2 = 800$ MHz for a spectral index of $\beta = 1.4$ (CHIME/FRB Collaboration et al. 2021). The energy limit at redshift z is given as $E_{\text{limit}} = 4\pi D_L^2(z) F_{\min} \nu_c k / (1+z)$ with a fluence sensitivity of $F_{\min} = 0.41$ Jy ms.

3. Methods

The Lynden-Bell's c^- method adopted in this paper has been widely used to analyze the luminosity distribution, isotropic energy distribution and redshift distribution of quasars (Lynden-Bell 1971; Efron & Petrosian 1992), Gamma-Ray Bursts (GRBs) (see, e.g., Yu et al. 2015; Petrosian et al. 2015; Liu et al. 2021; Dong et al. 2022) and FRBs (see, e.g., Deng et al. 2019). This method can break the degeneracy between the energy function and the formation rate, as long as the sample is large enough. If the energy function does not evolve with redshift, one can write $\Phi(E, z)$ as $\Phi(E, z) = \Psi(E)\rho(z)$, where $\Psi(E)$ is the isotropic energy function, $\rho(z)$ is the FRB formation rate at z . However, the energy function $\Psi(E(z))$ usually evolve with redshift z as $\Phi(E, z) = \Psi(E(z))\rho(z)$ instead of $\Phi(E, z) = \Psi(E)\rho(z)$, and this degeneracy can be eliminated by $g(z) = (1+z)^k$, so $\Phi(E, z) = \rho(z)\Psi(E(z)/g(z)) = \rho(z)\Psi(E_0)$, where $\Psi(E_0)$ is independent of redshift and represents the local energy function at $z = 0$. Then, the isotropic energy at redshift $z = 0$ is $E_0 = E(z)/g(z)$, with E_0 being independent of z . Observationally, the energy and the redshift of the CHIME FRBs are correlated as displayed in Figure 1. This may result from the instrumental effects and is not an intrinsic dependence. Thus, we need to reduce the observational bias and obtain the intrinsic correlation between E and z in advance.

Following some previous works (eg., Lynden-Bell 1971; Efron & Petrosian 1992; Deng et al. 2019; Liu et al. 2021; Zeng et al. 2021; Dong et al. 2022), we use the non-parametric method to derive the value of k (Efron & Petrosian 1992). For the i th data point (E_i, z_i) in the $E - z$ plane of Figure 1 (b), we define the set J_i and J'_i as

$$J_i = \{j \mid E_j > E_i, E_{j,\min}(z) < E_i (\text{or } z_j < z_{i,\max})\} \quad (3)$$

and

$$J'_i = \{j \mid z_j < z_i, z_{j,\max} > z_i (\text{or } E_j > E_{i,\min})\},$$

where $z_{i,\max}$ is the maximum redshift at which a FRB with the energy E_i can be detected by CHIME, the parameter $E_{i,\min}$ is the minimum energy which can be detected at redshift z_i . The region J_i is shown in Figure 1 (b) as a black rectangle, and the number of FRBs contained in this region is N_i . Similarly, the number of FRBs in J'_i (see Figure 1 (b) red rectangle) is denoted as M_i . Independence between E_i and z_i would make the number of the sample

$$R_i = \text{number} \{j \in J_i \mid z_j \leq z_i\} \quad (4)$$

uniformly distribute between 1 and N_i (Efron & Petrosian 1992). The expected mean and the variance are $E_i = (N_i + 1) / 2$ and $V_i = (N_i - 1)^2 / 12$, respectively.

The statistic τ used to test the dependence between energy and redshift is defined as

$$\tau \equiv \sum_i \frac{(R_i - E_i)}{\sqrt{V_i}}. \quad (5)$$

If energy and redshift don't have any correlations, the τ statistic gives $\tau = 0$, we can then make the transformation $E(z) \rightarrow E_0 = E(z)/g(z)$ and vary k until $\tau \rightarrow 0$, as well as the error is reported in 1σ confidence level (when $\tau = \pm 1$). Figure 2 (a) shows the variation of the τ value with k and returns $k = 5.23^{+0.19}_{-0.20}$ for $\tau = 0$ within 1σ confidence band. Then we apply the energy evolution form of $g(z) = (1+z)^{5.23}$ to remove the evolution effect, the de-evolved energy can be expressed as $E_0 = E(z)/(1+z)^{5.23}$ and the distribution of E_0 and z is shown in Figure 2 (b).

4. The energy function evolved or de-evolved with redshift

Through M_i and N_i depicted in Figure 1, we now derive the de-evolved energy function $\Psi(E_0)$ and the cumulative redshift distribution $\Phi(z)$ by the following nonparametric method (Lynden-Bell 1971; Efron & Petrosian 1992),

$$\Psi(E_{0,i}) = \prod_{j < i} \left(1 + \frac{1}{N_j}\right), \quad (6)$$

and

$$\phi(z_i) = \prod_{j < i} \left(1 + \frac{1}{M_j}\right), \quad (7)$$

where $j < i$ means that the energy $E_{0,j}$ is greater than $E_{0,i}$ in Eq. (6) and the FRB has a redshift z_j less than z_i in Eq. (7).

Subsequently, the FRB formation rate $\rho(z)$ can be determined by the following formula

$$\rho(z) = \frac{d\phi(z)}{dz} (1+z) \left(\frac{dV(z)}{dz}\right)^{-1}, \quad (8)$$

where the factor $(1+z)$ denotes the correction for the effect of cosmic time dilation. The differential comoving volume $dV(z)/dz$ is taken in the following form (Sun et al. 2015; Qiang et al. 2022)

$$\frac{dV(z)}{dz} = \frac{c}{H_0} \frac{4\pi D_L^2}{(1+z)^2 \sqrt{\Omega_m(1+z)^3 + \Omega_\Lambda}}, \quad (9)$$

for a flat Λ CDM model.

Using the new data set (N_j), one can obtain the normalized cumulative energy function $\Psi(E_0)$ in Figure 3, where the de-evolved energy function can be described by a broken power law as

$$\Psi(E_0) \propto \begin{cases} E_0^{-0.38 \pm 0.01}, & E_0 < E_b \\ E_0^{-2.01 \pm 0.12}, & E_0 \geq E_b \end{cases}, \quad (10)$$

where the broken energy is about $E_b = 2.1 \times 10^{40}$ erg, which is roughly consistent with some previous results (e.g., Deng et al. 2019). It is worth noting that the energy function only represents the "local" form at $z = 0$. The energy function at a given redshift z should be $\Psi(E_0)(1+z)^{5.23}$ in the observer frame and roughly break at $E_b(1+z)^{5.23}$.

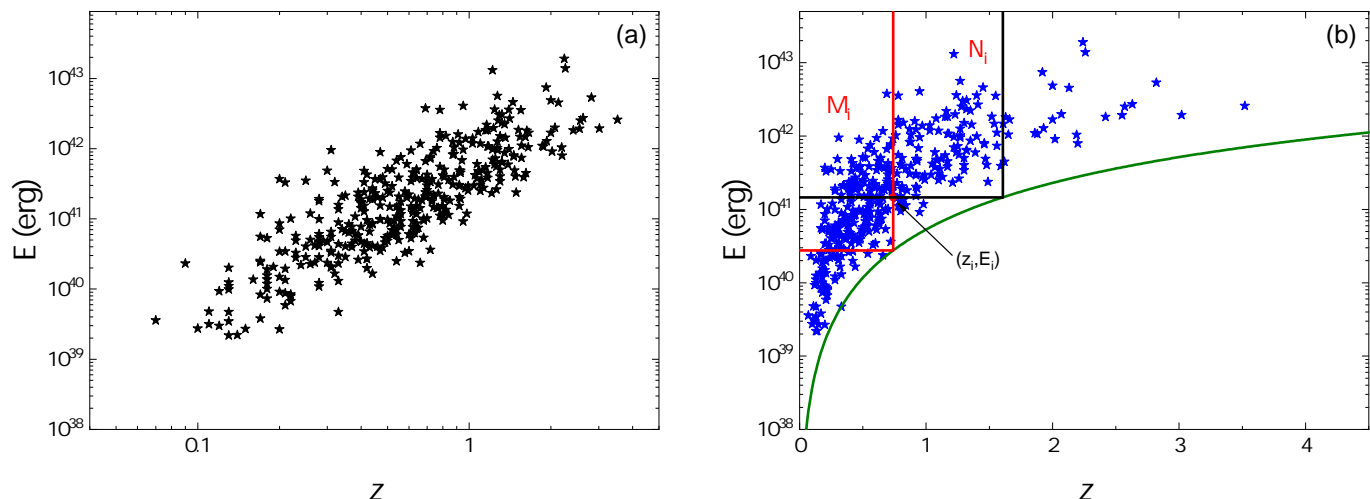


Fig. 1. The energy – redshift relations of 396 CHIME FRBs. The solid (green) curve shows the truncation boundary due to the instrumental fluence limit of 0.41 Jy ms. Panels (a) and (b) are different in the X-axis forms.

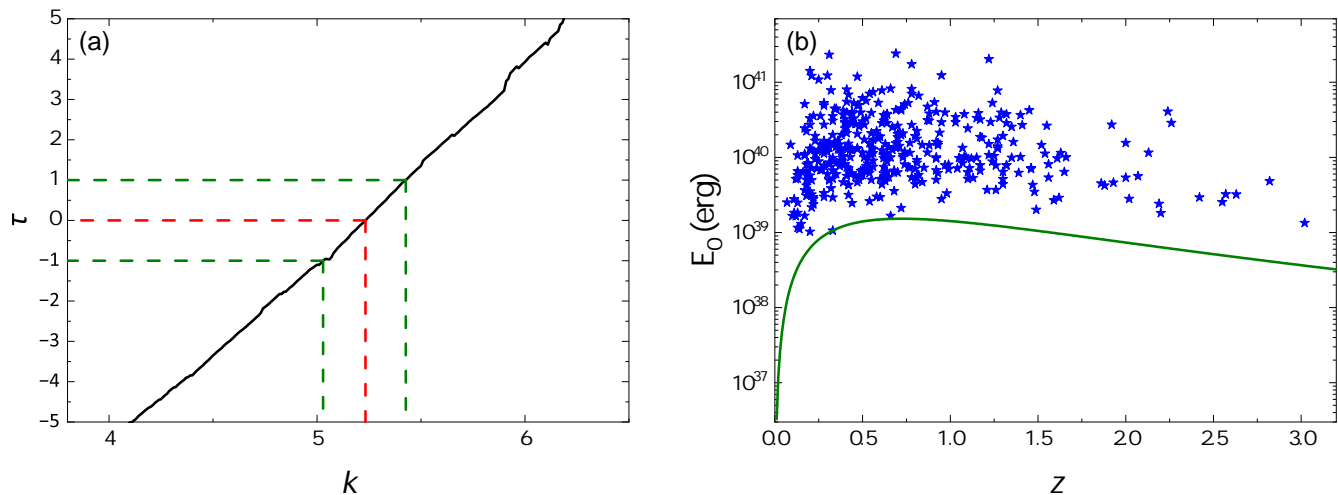


Fig. 2. (a): Variation of the τ parameter with the power law index k of the energy evolution. $\tau = 0$ means no correlation which gives the best value of $k = 5.23^{+0.19}_{-0.20}$ for the assumed power law form with 1σ confidence level. The red dashed line represents the best fit for $\tau = 0$ and the green dashed lines stand for the 1σ errors. (b): The distribution of the de-evolved energy $E_0 = E(z)/(1+z)^{5.23}$ of 396 FRBs above the truncation line or fluence limit denoted by the solid line.

5. The redshift distribution and formation rate evolution

Figure 4 (a) shows the normalized cumulative redshift distribution. We also get the differential distribution $d\phi(z)/dz$ of redshift in Figure 4 (b), where it is found that $(1+z)d\phi(z)/dz$ increases quickly at low redshift of $z \leq 0.5$, and then quickly decreases with redshift at the region of $z \geq 0.5$. Now, we use Eq. (8) to estimate the FRB formation rate and plot its relation with redshift in Figure 5. It can be obviously found that the formation rate of FRBs does not match the SFR at all. In particular, it exceeds the SFR at the low redshift end, which is very similar to the situation of GRBs discovered in many previous works (e.g. Dong et al. 2022, 2023). Observationally, the formation rate can be simply fitted by a power-law form of

$$\rho(z) = 29.516^{+2.11}_{-1.97} \times (1+z)^{-4.73 \pm 0.08} \quad (\text{M}_\odot \text{ Mpc}^{-3} \text{ yr}^{-1}), \quad (11)$$

as shown in Figure 5, where we can obviously find that the detection rate of FRBs does not match the SFR completely. The higher event rate of FRBs at lower redshifts demonstrates that FRBs most probably originate from older stellar populations in the nearby universe.

However, there are some evidences that FRBs might follow the global SFR of the universe. For example, FRB 20180916B and FRB 20201124A are detected from the star-forming regions (Marcote et al. 2020; Piro et al. 2021). Simultaneously, there are more evidences showing that at least parts of FRBs originate from magnetars (Bochenek et al. 2020; CHIME/FRB Collaboration et al. 2020; Heintz et al. 2020; Li & Zhang 2020; Mereghetti et al. 2020; Bochenek et al. 2021), which means that the formation rate of such kind of FRBs would follow the cosmic SFR (CHIME/FRB Collaboration et al. 2021; Zhang et al. 2021; James et al. 2022), like the samples of Parkes and ASKAP FRBs (Deng et al. 2019; Zhang et al. 2021; James et al. 2022).

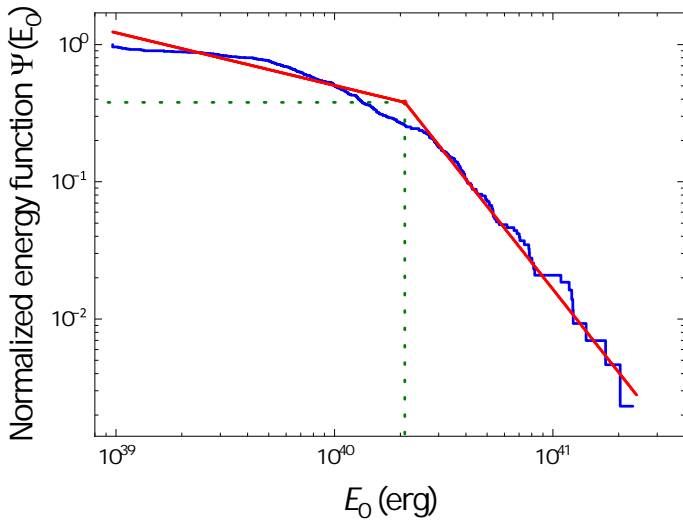


Fig. 3. The survival line (blue **step** line) of $\Psi(E_0)$ normalized to unity at the lowest energy is fitted by a broken power-law function (red solid line) with $\alpha_1 = -0.38 \pm 0.01$, $\alpha_2 = -2.01 \pm 0.12$, $E_b = 2.1 \times 10^{40}$ erg for a reduced Chi-square of $\chi^2 = 1.70$.

Noticeably, these previous results may be largely influenced by their limited FRB samples, causing the difference between our estimations of FRB rates especially in the low redshift range.

It is worth emphasizing that our sample is already large enough and the non-parametric method used in this work does not rely on any priori assumptions. Our conclusions support the recent finding that the CHIME FRB population does not track the SFR (Hashimoto et al. 2022; Qiang et al. 2022; Zhang & Zhang 2022). A significantly delayed FRB distribution tracking the star formation is also found to be reasonable (see, e.g., Cao et al. 2018a; Zhang et al. 2021; Qiang et al. 2022; Zevin et al. 2022; Panther et al. 2023; Gordon et al. 2023). This indicates that FRBs could be produced from multiple progenitor channels (e.g., Zhang & Zhang 2022; Gordon et al. 2023) or they might originate from distinct sub-populations (e.g., Good et al. 2023; Michilli et al. 2023; Nimmo et al. 2023; Zhang et al. 2023a), such as repeaters versus non-repeaters (Petroff et al. 2022), or long versus short FRBs (Li et al. 2021b). However, our recent investigations based on intensity function show that the repeating and non-repeating FRBs have similar event rates on the whole sky, hinting that both types of FRBs could share the same physical origin (Li et al. 2017; Zhang et al. 2022).

6. The local event rate of CHIME FRBs

According to Deng et al. (2019), the number of CHIME FRBs can be determined by

$$N = \frac{\Omega T}{4\pi} \int_{z_1}^{z_2} dz \int_{E_{min}}^{E_{max}} \frac{\Phi(E, z)}{1+z} \frac{dV}{dE}, \quad (12)$$

where z_1 and z_2 are the minimum and maximum redshifts respectively, E_{min} and E_{max} represent the lowest and highest energies of FRBs in the sample. $\Phi(E, z)$ is the total energy function defined in Section 3. When the variables E and z are separated, we can utilize $\Phi(E, z) = \Psi(E_0)\rho(z)$ and Equation (10) to rewrite the FRB number as

$$N = \frac{\Omega T}{4\pi} \int_{z_1}^{z_2} dz \int_{E_{0,min}}^{E_{0,max}} \frac{\Psi(E_0)\rho(z)}{1+z} \frac{dV}{dE_0}, \quad (13)$$

in which $\rho(z)$ and dV/dz have been individually given in Equations (8) and (9). The event rate of FRBs at a given redshift z can be expressed by $\rho(z) \propto \rho(0)(1+z)^{-4.73}$, where $\rho(0)$ denotes the local event rate of FRBs at redshift of $z = 0$. Here, we adopt the CHIME's effective observation period of 214.8 days (CHIME/FRB Collaboration et al. 2021), the field-of-view (FOV) of 200 deg² (CHIME/FRB Collaboration et al. 2018) and the total number of $N = 396$ to estimate the local FRB rate to be $\rho(0) \approx 1.25 \times 10^4 \text{ Gpc}^{-3}\text{yr}^{-1}$, which is roughly consistent with the rates of Parkes FRBs (Cao et al. 2018b), but slightly larger than that of ASKAP FRBs (Deng et al. 2019). Surprisingly, our result is slightly smaller than the local event rate of high energy CHIME FRBs (Zhang et al. 2023b). These discrepancies could be caused by the instrumental biases and some potential sample selection effects. Interestingly, it was shown by simulations that the local rate of White Dwarf (WD) mergers can be a few $10^4 \text{ Gpc}^{-3}\text{yr}^{-1}$ that is in good agreement with the observed SN Ia rate (Li et al. 2011). One can also convert the local CHIME FRB rate of our sample to a full sky rate as $\rho(0) \approx 396/93 \times 1.25 \times 10^4 \div 365 \approx 146 \text{ sky}^{-1}\text{day}^{-1}$ smaller than the official value of $\sim 820 \text{ sky}^{-1}\text{day}^{-1}$ and other rates (see e.g. Zhang et al. 2022), which may be biased by the larger fraction of low redshift FRBs or the nonuniformity of CHIME FRB samples. Note that the FOV of 200 deg² and 93 out of 396 FRBs within 1 Gpc have been utilized for the calculation.

7. CONCLUSIONS

We have applied the non-parametric method to investigate the energy function and formation rate of a homogeneous sample of 396 CHIME FRBs. Our results are model-independent and not suffered from the instrumental difference. The following principle conclusions can be drawn:

- We build a tight correlation between the total energies and redshifts of CHIME FRBs to be $E_0 \sim E(z)/(1+z)^{5.23}$ by using the Kendell's τ statistic method.
- After removing the evolution of energy with redshift, we derive the isotropic energy function that can be well fitted by a broken power-law form with two indices (-0.38 ± 0.01 and -2.01 ± 0.12) and a broken energy of $E_b \approx 2.1 \times 10^{40}$ erg.
- The FRB formation rate is found to decrease quickly. The best fit is $\rho(z) \propto (1+z)^{-4.71 \pm 0.12}$ for $z < 0.77$ and $\rho(z) \propto (1+z)^{-4.21 \pm 0.31}$ for $z \geq 0.77$, and also we have obtained the local FRB rate as $\rho(0) \approx 1.25 \times 10^4 \text{ Gpc}^{-3}\text{yr}^{-1}$, which is roughly consistent with some previous results.
- We find that the FRB formation rate does not match with the SFR and the former exceeds the later at lower redshifts. It indicates that most FRBs are probably contributed by the older stellar populations in the universe.

Acknowledgements. This work was supported in part by National Natural Science Foundation of China (grant Nos. U2031118, 12041306, 11988101), the National Key R&D Program of China (2021YFA0718500), the National SKA Program of China No. 2020SKA0120300 and the Natural Science Foundations (ZR2018MA030, XKJJC201901). We also acknowledge the usage of the archive data in the First CHIME/FRB Catalog (<https://www.chime-frb.ca/catalog>).

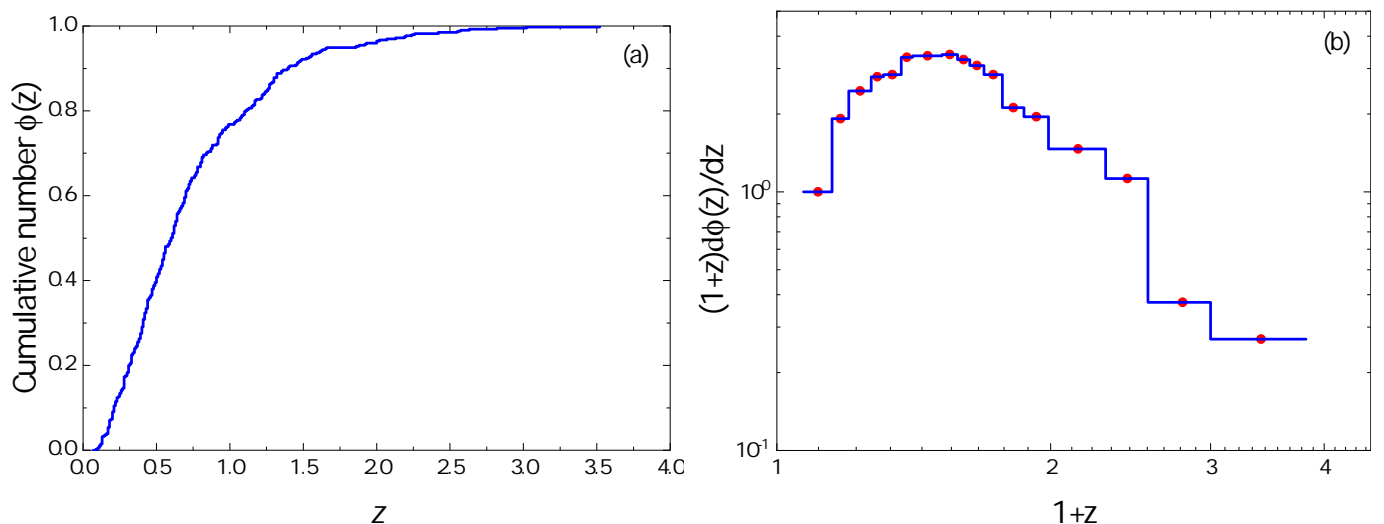


Fig. 4. (a): Cumulative redshift distribution of FRBs. (b): The evolution of $(1+z)d\phi(z)/dz$ as a function of redshift z , which is normalized to unity at the first point.

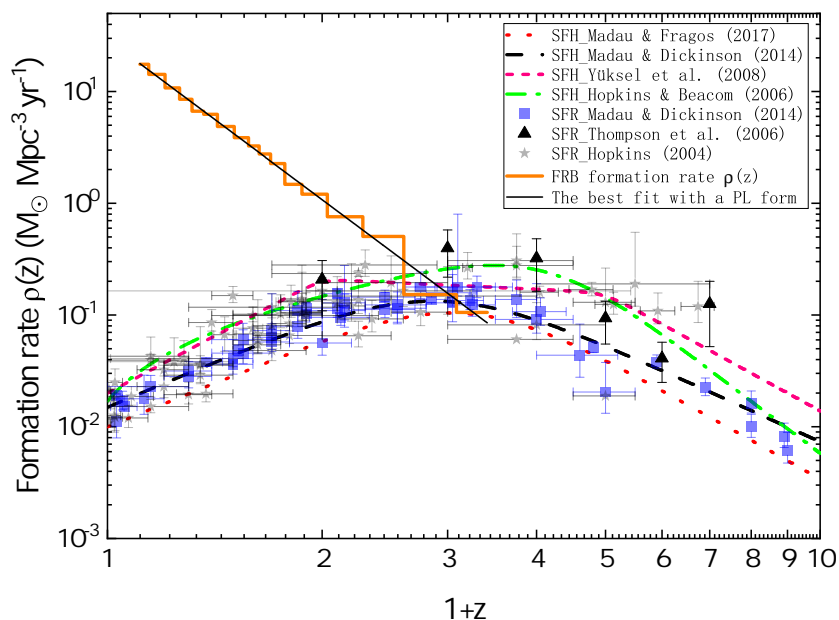


Fig. 5. The formation rate $\rho(z)$ of CHIME FRBs and the SFR versus redshift. The red dotted line (Madau & Fragos 2017), black dashed line (Madau & Dickinson 2014), pink short dashed line (Yüksel et al. 2008) and green dash-dotted line (Hopkins & Beacom 2006) are different SFR models. Blue squares, black uptriangles and gray stars represent the observed SFR taken from Madau & Dickinson (2014), Thompson et al. (2006) and Hopkins (2004), respectively.

References

- Ai, S., Gao, H., & Zhang, B. 2021, *ApJ*, 906, L5
- Arcus, W. R., Macquart, J. P., Sammons, M. W., James, C. W., & Ekers, R. D. 2021, *MNRAS*, 501, 5319
- Bandura, K., Addison, G. E., Amiri, M., et al. 2014, in *Society of Photo-Optical Instrumentation Engineers (SPIE) Conference Series*, Vol. 9145, *Ground-based and Airborne Telescopes V*, ed. L. M. Stepp, R. Gilmozzi, & H. J. Hall, 914522
- Bannister, K. W., Deller, A. T., Phillips, C., et al. 2019, *Science*, 365, 565
- Bassa, C. G., Tendulkar, S. P., Adams, E. A. K., et al. 2017, *ApJ*, 843, L8
- Bhandari, S., Gordon, A. C., Scott, D. R., et al. 2023, *ApJ*, 948, 67
- Bhardwaj, M., Gaensler, B. M., Kaspi, V. M., et al. 2021, *ApJ*, 910, L18
- Bhattacharya, M. & Kumar, P. 2020, *ApJ*, 899, 124
- Bochenek, C. D., Ravi, V., Belov, K. V., et al. 2020, *Nature*, 587, 59
- Bochenek, C. D., Ravi, V., & Dong, D. 2021, *ApJ*, 907, L31
- Caleb, M., Stappers, B. W., Rajwade, K., & Flynn, C. 2019, *MNRAS*, 484, 5500
- Cao, X.-F., Xiao, M., & Xiao, F. 2017, *Research in Astronomy and Astrophysics*, 17, 14
- Cao, X.-F., Yu, Y.-W., & Zhou, X. 2018a, *ApJ*, 858, 89
- Cao, X.-F., Yu, Y.-W., & Zhou, X. 2018b, *ApJ*, 858, 89
- Chen, B. H., Hashimoto, T., Goto, T., et al. 2022, *MNRAS*, 509, 1227
- CHIME/FRB Collaboration, Amiri, M., Andersen, B. C., et al. 2021, *ApJS*, 257, 59
- CHIME/FRB Collaboration, Amiri, M., Bandura, K., et al. 2018, *ApJ*, 863, 48
- CHIME/FRB Collaboration, Andersen, B. C., Bandura, K. M., et al. 2020, *Nature*, 587, 54
- Deng, C.-M., Cai, Y., Wu, X.-F., & Liang, E.-W. 2018, *Phys. Rev. D*, 98, 123016
- Deng, C.-M., Wei, J.-J., & Wu, X.-F. 2019, *Journal of High Energy Astrophysics*, 23, 1
- Dong, X. F., Li, X. J., Zhang, Z. B., & Zhang, X. L. 2022, *MNRAS*[arXiv:2103.16347]
- Dong, X. F., Zhang, Z. B., Li, Q. M., Huang, Y. F., & Bian, K. 2023, *ApJ*, 958, 37
- Efron, B. & Petrosian, V. 1992, *ApJ*, 399, 345
- Efron, B. & Petrosian, V. 1998, *Journal of the American Statistical Association*, 94, 824
- Fong, W.-f., Dong, Y., Leja, J., et al. 2021, *ApJ*, 919, L23
- Gajjar, V., Siemion, A. P. V., Price, D. C., et al. 2018, *ApJ*, 863, 2

- Geng, J., Li, B., & Huang, Y. 2021, *The Innovation*, 2, 100152
- Good, D. C., Chawla, P., Fonseca, E., et al. 2023, *ApJ*, 944, 70
- Gordon, A. C., Fong, W.-f., Kilpatrick, C. D., et al. 2023, arXiv e-prints, arXiv:2302.05465
- Hashimoto, T., Goto, T., Chen, B. H., et al. 2022, *MNRAS*, 511, 1961
- Hashimoto, T., Goto, T., On, A. Y. L., et al. 2020a, *MNRAS*, 498, 3927
- Hashimoto, T., Goto, T., Wang, T.-W., et al. 2020b, *MNRAS*, 494, 2886
- Heintz, K. E., Prochaska, J. X., Simha, S., et al. 2020, *ApJ*, 903, 152
- Hopkins, A. M. 2004, *ApJ*, 615, 209
- Hopkins, A. M. & Beacom, J. F. 2006, *ApJ*, 651, 142
- James, C. W., Prochaska, J. X., Macquart, J. P., et al. 2022, *MNRAS*, 510, L18
- Kirsten, F., Marcote, B., Nimmo, K., et al. 2022, *Nature*, 602, 585
- Kirsten, F., Ould-Boukattine, O., Herrmann, W., et al. 2023, arXiv e-prints, arXiv:2306.15505
- Kremer, K., Piro, A. L., & Li, D. 2021, *ApJ*, 917, L11
- Kumar, P., Shannon, R. M., Osłowski, S., et al. 2019, *ApJ*, 887, L30
- Law, C. J., Sharma, K., Ravi, V., et al. 2023, arXiv e-prints, arXiv:2307.03344
- Li, C. K., Lin, L., Xiong, S. L., et al. 2021a, *Nature Astronomy*, 5, 378
- Li, L.-B., Huang, Y.-F., Zhang, Z.-B., Li, D., & Li, B. 2017, *Research in Astronomy and Astrophysics*, 17, 6
- Li, W., Chornock, R., Leaman, J., et al. 2011, *MNRAS*, 412, 1473
- Li, X. J., Dong, X. F., Zhang, Z. B., & Li, D. 2021b, *ApJ*, 923, 230
- Li, Y. & Zhang, B. 2020, *ApJ*, 899, L6
- Lin, L., Zhang, C. F., Wang, P., et al. 2020, *Nature*, 587, 63
- Liu, Z.-Y., Zhang, F.-W., & Zhu, S.-Y. 2021, *Research in Astronomy and Astrophysics*, 21, 254
- Locatelli, N., Ronchi, M., Ghirlanda, G., & Ghisellini, G. 2019, *A&A*, 625, A109
- Lorimer, D. R., Karastergiou, A., McLaughlin, M. A., & Johnston, S. 2013, *MNRAS*, 436, L5
- Luo, R., Lee, K., Lorimer, D. R., & Zhang, B. 2018, *MNRAS*, 481, 2320
- Luo, R., Men, Y., Lee, K., et al. 2020, *MNRAS*, 494, 665
- Lynden-Bell, D. 1971, *MNRAS*, 155, 95
- Macquart, J. P. & Ekers, R. D. 2018, *MNRAS*, 474, 1900
- Madau, P. & Dickinson, M. 2014, *ARA&A*, 52, 415
- Madau, P. & Fragos, T. 2017, *ApJ*, 840, 39
- Marcote, B., Nimmo, K., Hessels, J. W. T., et al. 2020, *Nature*, 577, 190
- Marshall, H. L., Tananbaum, H., Avni, Y., & Zamorani, G. 1983, *ApJ*, 269, 35
- Mereghetti, S., Savchenko, V., Ferrigno, C., et al. 2020, *ApJ*, 898, L29
- Michilli, D., Bhardwaj, M., Brar, C., et al. 2023, *ApJ*, 950, 134
- Mottez, F. & Zarka, P. 2014, *A&A*, 569, A86
- Nimmo, K., Hessels, J. W. T., Snelders, M. P., et al. 2023, *MNRAS*, 520, 2281
- Niu, C. H., Aggarwal, K., Li, D., et al. 2022, *Nature*, 606, 873
- Panther, F. H., Anderson, G. E., Bhandari, S., et al. 2023, *MNRAS*, 519, 2235
- Pastor-Marazuela, I., Connor, L., van Leeuwen, J., et al. 2021, *Nature*, 596, 505
- Petroff, E., Hessels, J. W. T., & Lorimer, D. R. 2022, *A&A Rev.*, 30, 2
- Petroff, E. & Yaron, O. 2020, *Transient Name Server AstroNote*, 160, 1
- Petrosian, V., Kitanidis, E., & Kocevski, D. 2015, *ApJ*, 806, 44
- Piro, L., Bruni, G., Troja, E., et al. 2021, *A&A*, 656, L15
- Planck Collaboration, Ade, P. A. R., Aghanim, N., et al. 2016, *A&A*, 594, A13
- Platts, E., Weltman, A., Walters, A., et al. 2019, *Phys. Rep.*, 821, 1
- Pleunis, Z., Good, D. C., Kaspi, V. M., et al. 2021a, *ApJ*, 923, 1
- Pleunis, Z., Michilli, D., Bassa, C. G., et al. 2021b, *ApJ*, 911, L3
- Popov S., B. & Pshirkov M., S. 2023, arXiv e-prints, arXiv:2303.05591
- Prochaska, J. X., Macquart, J.-P., McQuinn, M., et al. 2019, *Science*, 366, 231
- Qiang, D.-C., Li, S.-L., & Wei, H. 2022, *J. Cosmology Astropart. Phys.*, 2022, 040
- Ravi, V. 2019, *MNRAS*, 482, 1966
- Ravi, V., Law, C. J., Li, D., et al. 2022, *MNRAS*, 513, 982
- Ridnaia, A., Svinkin, D., Frederiks, D., et al. 2021, *Nature Astronomy*, 5, 372
- Spanakis-Misirilis, A. 2021, *FRBSTATS: A web-based platform for visualization of fast radio burst properties*
- Sun, H., Zhang, B., & Li, Z. 2015, *ApJ*, 812, 33
- Tang, L., Lin, H.-N., & Li, X. 2023, *Chinese Physics C*, 47, 085105
- Tavani, M., Casentini, C., Ursi, A., et al. 2021, *Nature Astronomy*, 5, 401
- Tendulkar, S. P., Bassa, C. G., Cordes, J. M., et al. 2017, *ApJ*, 834, L7
- Tendulkar, S. P., Gil de Paz, A., Kirichenko, A. Y., et al. 2021, *ApJ*, 908, L12
- Thompson, R. I., Eisenstein, D., Fan, X., et al. 2006, *ApJ*, 647, 787
- Wada, T. & Ioka, K. 2023, *MNRAS*, 519, 4094
- Xiao, D., Wang, F., & Dai, Z. 2021, *Science China Physics, Mechanics, and Astronomy*, 64, 249501
- Xu, H., Niu, J. R., Chen, P., et al. 2021, arXiv e-prints, arXiv:2111.11764
- Yu, H., Wang, F. Y., Dai, Z. G., & Cheng, K. S. 2015, *ApJS*, 218, 13
- Yüksel, H., Kistler, M. D., Beacom, J. F., & Hopkins, A. M. 2008, *ApJ*, 683, L5
- Zeng, H., Petrosian, V., & Yi, T. 2021, *ApJ*, 913, 120
- Zevin, M., Nugent, A. E., Adhikari, S., et al. 2022, *ApJ*, 940, L18
- Zhang, B. 2017, *ApJ*, 836, L32
- Zhang, B. 2018, *ApJ*, 867, L21
- Zhang, B. 2020, *Nature*, 587, 45
- Zhang, G. Q. & Wang, F. Y. 2019, *MNRAS*, 487, 3672
- Zhang, K., Li, L., Zhang, Z., et al. 2022, *Universe*, 8, 355
- Zhang, R. C. & Zhang, B. 2022, *ApJ*, 924, L14
- Zhang, R. C., Zhang, B., Li, Y., & Lorimer, D. R. 2021, *MNRAS*, 501, 157
- Zhang, Y.-K., Li, D., Feng, Y., et al. 2023a, arXiv e-prints, arXiv:2305.18052
- Zhang, Z.-L., Yu, Y.-W., & Cao, X.-F. 2023b, *A&A*, 675, A66

Appendix A: The selected CHIME FRB sample

Table A.1. The data are taken from <https://www.chime-frb.ca/catalog> (CHIME/FRB Collaboration et al. 2021)

TNS name	DM_E (pc cm^{-3})	Fluence (Jy ms)	z	E (erg)	Repeat
FRB20190221D	284.2	1.13	0.33	1.30×10^{40}	NO
FRB20190222B	464.4	4.40	0.54	1.48×10^{41}	NO
FRB20190224B	788.0	4.50	0.92	4.88×10^{41}	NO
FRB20190430B	2583.0	1.52	3.02	1.94×10^{42}	NO
FRB20190628C	1649.6	2.45	1.93	1.28×10^{42}	NO
FRB20190629A	468.7	3.05	0.55	1.07×10^{41}	NO
FRB20181014C	692.3	1.48	0.81	1.22×10^{41}	NO
FRB20190128C	239.3	5.90	0.28	4.75×10^{40}	NO
FRB20190204A	413.5	1.50	0.48	3.91×10^{40}	NO
FRB20190322B	530.0	2.04	0.62	9.32×10^{40}	NO
FRB20181214B	1078.7	1.23	1.26	2.63×10^{41}	NO
FRB20190117C	812.6	0.79	0.95	9.18×10^{40}	NO
FRB20190328A	1251.8	2.66	1.46	7.76×10^{41}	NO
FRB20190429B	253.5	5.00	0.30	4.68×10^{40}	NO
FRB20180921A	359.2	2.30	0.42	4.47×10^{40}	NO
FRB20181203C	2407.1	4.80	2.82	5.36×10^{42}	NO
FRB20190220A	175.2	0.68	0.20	2.66×10^{39}	NO
FRB20190308B	111.5	1.39	0.13	2.19×10^{39}	NO
FRB20181124A	1074.1	2.60	1.26	5.55×10^{41}	NO
FRB20181202C	430.7	3.40	0.50	9.69×10^{40}	NO
FRB20190115A	835.3	0.95	0.98	1.18×10^{41}	NO
FRB20190301D	1107.6	1.50	1.30	3.42×10^{41}	NO
FRB20180906A	340.0	2.70	0.40	4.72×10^{40}	NO
FRB20180920B	430.2	1.70	0.50	4.84×10^{40}	NO
FRB20181222D	1385.9	1.23	1.62	4.46×10^{41}	NO
FRB20190103D	1880.3	1.17	2.20	7.96×10^{41}	NO
FRB20190226A	510.3	1.42	0.60	6.04×10^{40}	NO
FRB20190226C	783.3	1.41	0.92	1.53×10^{41}	NO
FRB20190419A	377.7	0.77	0.44	1.66×10^{40}	NO
FRB20190529A	539.0	1.45	0.63	6.86×10^{40}	NO
FRB20190601D	604.6	5.70	0.71	3.51×10^{41}	NO
FRB20180906B	3006.7	1.50	3.52	2.57×10^{42}	NO
FRB20181013E	264.5	2.03	0.31	2.04×10^{40}	NO
FRB20190420C	594.2	4.13	0.69	2.39×10^{41}	NO
FRB20181018A	1008.5	5.80	1.18	1.08×10^{42}	NO
FRB20181118A	525.9	10.00	0.62	4.57×10^{41}	NO
FRB20190217B	800.4	6.00	0.94	6.82×10^{41}	NO
FRB20190304C	542.9	1.32	0.63	6.25×10^{40}	NO
FRB20190403A	464.6	3.19	0.54	1.08×10^{41}	NO
FRB20190630C	1592.3	2.27	1.86	1.10×10^{42}	NO
FRB20181218B	583.8	1.80	0.68	1.01×10^{41}	NO
FRB20190105A	337.2	3.50	0.39	5.79×10^{40}	NO
FRB20190113A	250.0	5.60	0.29	4.87×10^{40}	NO
FRB20190402A	1265.3	1.34	1.48	4.02×10^{41}	NO
FRB20190403D	550.5	1.75	0.64	8.58×10^{40}	NO
FRB20190605D	1607.7	2.16	1.88	1.07×10^{42}	NO
FRB20190628A	716.0	1.28	0.84	1.14×10^{41}	NO
FRB20180909A	358.8	1.02	0.42	1.98×10^{40}	NO
FRB20181128C	569.2	3.40	0.67	1.84×10^{41}	NO
FRB20181214F	2065.5	2.21	2.42	1.82×10^{42}	NO
FRB20181216A	396.0	1.70	0.46	4.04×10^{40}	NO
FRB20181222C	1058.5	2.90	1.24	5.98×10^{41}	NO

:

— *Continued from previous page*

TNS name	DM_E (pc cm^{-3})	Fluence (Jy ms)	z	E (erg)	Repeat
FRB20190201A	179.6	3.10	0.21	1.35×10^{40}	NO
FRB20190411A	399.8	1.41	0.47	3.51×10^{40}	NO
FRB20190609C	367.6	1.91	0.43	3.91×10^{40}	NO
FRB20180916C	2179.0	2.10	2.55	1.92×10^{42}	NO
FRB20181015A	522.3	3.40	0.61	1.50×10^{41}	NO
FRB20181228C	465.1	0.74	0.54	2.50×10^{40}	NO
FRB20181229B	359.7	4.90	0.42	9.53×10^{40}	NO
FRB20190203C	340.8	4.40	0.40	7.69×10^{40}	NO
FRB20190218B	466.3	5.90	0.55	2.07×10^{41}	NO
FRB20190422B	943.3	1.57	1.10	2.51×10^{41}	NO
FRB20190430A	281.4	7.70	0.33	8.85×10^{40}	NO
FRB20181119E	949.5	2.20	1.11	3.58×10^{41}	NO
FRB20181224D	658.8	1.95	0.77	1.43×10^{41}	NO
FRB20190409C	631.6	2.17	0.74	1.46×10^{41}	NO
FRB20180907C	546.8	1.48	0.64	7.25×10^{40}	NO
FRB20180925A	167.1	8.70	0.20	3.40×10^{40}	NO
FRB20181019B	565.4	2.70	0.66	1.42×10^{41}	NO
FRB20190214A	427.9	8.80	0.50	2.51×10^{41}	NO
FRB20190317C	544.7	7.80	0.64	3.82×10^{41}	NO
FRB20190320C	321.7	3.14	0.38	4.91×10^{40}	NO
FRB20190403G	700.0	1.59	0.82	1.34×10^{41}	NO
FRB20190621B	1030.5	1.19	1.21	2.33×10^{41}	NO
FRB20181019C	462.4	2.10	0.54	7.09×10^{40}	NO
FRB20190114A	849.3	2.30	0.99	2.92×10^{41}	NO
FRB20190116D	1085.5	4.70	1.27	1.02×10^{42}	NO
FRB20190127B	614.6	11.40	0.72	7.23×10^{41}	NO
FRB20190323C	357.5	1.38	0.42	2.68×10^{40}	NO
FRB20190530A	416.2	1.69	0.49	4.61×10^{40}	NO
FRB20190701C	915.8	2.50	1.07	3.76×10^{41}	NO
FRB20181020A	1040.3	4.90	1.22	9.77×10^{41}	NO
FRB20190109B	106.9	3.00	0.13	4.72×10^{39}	NO
FRB20181013B	191.7	21.00	0.22	1.01×10^{41}	NO
FRB20181030C	595.7	5.50	0.70	3.28×10^{41}	NO
FRB20181213C	350.2	1.86	0.41	3.43×10^{40}	NO
FRB20190122A	1166.6	5.70	1.36	1.43×10^{42}	NO
FRB20190224A	752.9	8.50	0.88	8.36×10^{41}	NO
FRB20190325C	609.4	3.83	0.71	2.36×10^{41}	NO
FRB20190326A	242.6	1.51	0.28	1.22×10^{40}	NO
FRB20190329A	100.8	2.24	0.12	2.98×10^{39}	NO
FRB20181012B	681.7	1.44	0.80	1.15×10^{41}	NO
FRB20181129B	343.8	9.50	0.40	1.66×10^{41}	NO
FRB20190128A	652.5	2.00	0.76	1.43×10^{41}	NO
FRB20190603B	404.0	6.20	0.47	1.54×10^{41}	NO
FRB20181102A	258.8	2.52	0.30	2.36×10^{40}	NO
FRB20190116E	1362.6	1.12	1.59	3.91×10^{41}	NO
FRB20190403F	596.8	7.10	0.70	4.24×10^{41}	NO
FRB20180925B	628.2	2.70	0.73	1.77×10^{41}	NO
FRB20190614C	531.7	2.91	0.62	1.33×10^{41}	NO
FRB20190627D	1870.2	1.54	2.19	1.04×10^{42}	NO
FRB20190415A	596.7	3.70	0.70	2.21×10^{41}	NO
FRB20190625C	366.1	4.02	0.43	8.23×10^{40}	NO
FRB20190701A	582.8	1.70	0.68	9.52×10^{40}	NO
FRB20180907E	352.9	6.90	0.41	1.27×10^{41}	NO
FRB20181117A	921.2	3.10	1.08	4.76×10^{41}	NO
FRB20181122A	466.7	1.42	0.55	4.99×10^{40}	NO
FRB20190131B	1770.1	3.30	2.07	1.98×10^{42}	NO
FRB20190212C	994.1	12.20	1.16	2.18×10^{42}	NO

— *Continued from previous page*

TNS name	DM_E (pc cm^{-3})	Fluence (Jy ms)	z	E (erg)	Repeat
FRB20180907D	1391.1	4.90	1.63	1.80×10^{42}	NO
FRB20181213B	596.0	1.70	0.70	1.01×10^{41}	NO
FRB20190110B	440.6	1.90	0.52	5.90×10^{40}	NO
FRB20190409B	237.8	6.80	0.28	5.48×10^{40}	NO
FRB20181223B	540.2	4.10	0.63	1.94×10^{41}	NO
FRB20190628B	361.5	1.39	0.42	2.70×10^{40}	NO
FRB20180915B	154.7	3.80	0.18	1.19×10^{40}	NO
FRB20181217A	1107.4	1.76	1.30	4.02×10^{41}	NO
FRB20190320D	1097.5	11.40	1.28	2.52×10^{42}	NO
FRB20190623C	1001.0	5.90	1.17	1.08×10^{42}	NO
FRB20181013C	967.2	1.64	1.13	2.77×10^{41}	NO
FRB20181017B	263.7	6.50	0.31	6.52×10^{40}	NO
FRB20181228A	714.5	4.00	0.84	3.56×10^{41}	NO
FRB20190129A	432.7	5.00	0.51	1.49×10^{41}	NO
FRB20190211B	176.2	1.35	0.21	5.86×10^{39}	NO
FRB20190316A	477.0	2.53	0.56	9.25×10^{40}	NO
FRB20190412B	110.9	12.80	0.13	2.02×10^{40}	NO
FRB20181230B	1052.4	9.70	1.23	1.97×10^{42}	NO
FRB20190518B	887.7	2.10	1.04	2.97×10^{41}	NO
FRB20190515D	378.3	8.80	0.44	1.90×10^{41}	NO
FRB20190223A	331.1	1.58	0.39	2.61×10^{40}	NO
FRB20181128B	423.0	1.95	0.49	5.32×10^{40}	NO
FRB20181224C	541.0	9.60	0.63	4.54×10^{41}	NO
FRB20181230D	183.4	2.00	0.21	8.69×10^{39}	NO
FRB20190325A	308.3	4.60	0.36	6.39×10^{40}	NO
FRB20180915A	199.1	6.20	0.23	3.27×10^{40}	NO
FRB20181220B	204.2	3.80	0.24	2.20×10^{40}	NO
FRB20190206A	146.9	9.10	0.17	2.52×10^{40}	NO
FRB20180920A	394.9	8.50	0.46	2.02×10^{41}	NO
FRB20190414A	791.8	1.74	0.93	1.93×10^{41}	NO
FRB20181014D	347.1	18.00	0.41	3.32×10^{41}	NO
FRB20190116F	270.1	1.54	0.32	1.66×10^{40}	NO
FRB20190124E	225.8	7.30	0.26	5.01×10^{40}	NO
FRB20190131C	474.8	2.10	0.56	7.68×10^{40}	NO
FRB20190221A	170.9	2.33	0.20	9.12×10^{39}	NO
FRB20190414B	468.7	3.80	0.55	1.34×10^{41}	NO
FRB20190218A	1253.7	1.65	1.47	4.88×10^{41}	NO
FRB20190221B	227.6	5.60	0.27	4.17×10^{40}	NO
FRB20181230E	987.2	10.40	1.15	1.83×10^{42}	NO
FRB20180918A	1374.0	4.10	1.61	1.47×10^{42}	NO
FRB20181224B	659.7	3.10	0.77	2.28×10^{41}	NO
FRB20190101B	1089.9	4.40	1.27	9.55×10^{41}	NO
FRB20181101A	1327.8	10.70	1.55	3.54×10^{42}	NO
FRB20181230A	701.2	18.00	0.82	1.52×10^{42}	NO
FRB20190128B	191.0	1.64	0.22	7.87×10^{39}	NO
FRB20190313B	1131.4	2.74	1.32	6.46×10^{41}	NO
FRB20181201B	825.3	2.24	0.97	2.72×10^{41}	NO
FRB20181230C	1000.3	2.10	1.17	3.83×10^{41}	NO
FRB20190124A	1099.3	13.40	1.29	3.01×10^{42}	NO
FRB20190621C	544.6	2.38	0.64	1.17×10^{41}	NO
FRB20190124B	419.8	11.70	0.49	3.19×10^{41}	NO
FRB20190409A	1707.5	8.70	2.00	4.88×10^{42}	NO
FRB20190416A	2248.1	2.80	2.63	2.72×10^{42}	NO
FRB20190323A	784.7	2.71	0.92	2.94×10^{41}	NO
FRB20190423C	795.1	4.37	0.93	4.85×10^{41}	NO
FRB20190527A	550.9	10.10	0.64	4.95×10^{41}	NO
FRB20190317E	666.6	7.30	0.78	5.52×10^{41}	NO

— *Continued from previous page*

TNS name	DM _E (pc cm ⁻³)	Fluence (Jy ms)	<i>z</i>	E (erg)	Repeat
FRB20190417B	1126.2	9.90	1.32	2.33×10 ⁴²	NO
FRB20190518D	148.5	3.00	0.17	8.31×10 ³⁹	NO
FRB20180923C	144.9	1.37	0.17	3.80×10 ³⁹	NO
FRB20181022C	478.6	3.20	0.56	1.17×10 ⁴¹	NO
FRB20190701B	687.6	1.90	0.80	1.52×10 ⁴¹	NO
FRB20190601A	2194.9	2.70	2.57	2.51×10 ⁴²	NO
FRB20190604D	996.4	2.48	1.17	4.52×10 ⁴¹	NO
FRB20190701E	848.1	2.00	0.99	2.54×10 ⁴¹	NO
FRB20180907A	785.2	2.80	0.92	3.04×10 ⁴¹	NO
FRB20190516B	1202.1	9.90	1.41	2.68×10 ⁴²	NO
FRB20190624A	936.0	3.01	1.09	4.71×10 ⁴¹	NO
FRB20180907B	620.1	2.90	0.73	1.90×10 ⁴¹	NO
FRB20190217A	687.4	1.19	0.80	9.51×10 ⁴⁰	NO
FRB20181022E	264.2	2.08	0.31	2.09×10 ⁴⁰	NO
FRB20181228B	528.7	1.67	0.62	7.63×10 ⁴⁰	NO
FRB20190214C	511.0	5.20	0.60	2.21×10 ⁴¹	NO
FRB20190110C	186.3	1.40	0.22	6.72×10 ³⁹	NO
FRB20190303C	1066.6	3.46	1.25	7.26×10 ⁴¹	NO
FRB20190411B	1194.3	3.70	1.40	9.88×10 ⁴¹	NO
FRB20181127A	898.1	2.90	1.05	4.19×10 ⁴¹	NO
FRB20190103B	354.0	12.90	0.41	2.38×10 ⁴¹	NO
FRB20190117D	1155.5	3.50	1.35	8.65×10 ⁴¹	NO
FRB20190320A	470.2	4.40	0.55	1.55×10 ⁴¹	NO
FRB20190607B	151.1	3.20	0.18	1.00×10 ⁴⁰	NO
FRB20181027A	663.7	22.00	0.78	1.66×10 ⁴²	NO
FRB20190420A	543.4	3.11	0.64	1.52×10 ⁴¹	NO
FRB20190423B	102.3	7.00	0.12	9.32×10 ³⁹	NO
FRB20181116B	373.5	1.92	0.44	4.13×10 ⁴⁰	NO
FRB20180919B	527.4	3.00	0.62	1.37×10 ⁴¹	NO
FRB20180923A	119.4	1.20	0.14	2.21×10 ³⁹	NO
FRB20181202B	792.2	4.10	0.93	4.55×10 ⁴¹	NO
FRB20181213A	630.1	3.20	0.74	2.16×10 ⁴¹	NO
FRB20190409D	1245.4	2.74	1.46	7.99×10 ⁴¹	NO
FRB20190222C	494.5	0.83	0.58	3.28×10 ⁴⁰	NO
FRB20190208C	188.7	1.74	0.22	8.35×10 ³⁹	NO
FRB20180917B	813.9	8.30	0.95	9.65×10 ⁴¹	NO
FRB20181226E	239.9	1.35	0.28	1.09×10 ⁴⁰	NO
FRB20190609D	454.2	2.36	0.53	7.64×10 ⁴⁰	NO
FRB20190604E	1192.6	2.26	1.39	5.94×10 ⁴¹	NO
FRB20181123A	694.9	2.50	0.81	2.05×10 ⁴¹	NO
FRB20190519E	666.3	1.46	0.78	1.10×10 ⁴¹	NO
FRB20181117B	473.2	11.00	0.55	3.86×10 ⁴¹	NO
FRB20190104A	397.9	3.90	0.47	9.70×10 ⁴⁰	NO
FRB20190621D	596.8	4.30	0.70	2.57×10 ⁴¹	NO
FRB20181222E	268.1	5.50	0.31	5.52×10 ⁴⁰	NO
FRB20190101A	830.3	11.30	0.97	1.37×10 ⁴²	NO
FRB20181201A	670.4	18.90	0.78	1.43×10 ⁴²	NO
FRB20190320B	451.8	1.90	0.53	6.15×10 ⁴⁰	NO
FRB20181118B	369.2	3.20	0.43	6.55×10 ⁴⁰	NO
FRB20190424A	723.2	1.99	0.85	1.82×10 ⁴¹	NO
FRB20180924A	1047.3	3.50	1.22	6.98×10 ⁴¹	NO
FRB20181014A	1128.2	2.70	1.32	6.36×10 ⁴¹	NO
FRB20181214D	1151.3	9.00	1.35	2.23×10 ⁴²	NO
FRB20181231C	520.6	1.20	0.61	5.29×10 ⁴⁰	NO
FRB20190115B	684.5	5.20	0.80	4.16×10 ⁴¹	NO
FRB20190328C	408.2	14.90	0.48	3.88×10 ⁴¹	NO
FRB20190425B	979.0	3.10	1.15	5.44×10 ⁴¹	NO

— Continued from previous page

TNS name	DM_E (pc cm^{-3})	Fluence (Jy ms)	z	E (erg)	Repeat
FRB20181125A	234.2	3.20	0.27	2.38×10^{40}	NO
FRB20181129C	475.7	3.60	0.56	1.32×10^{41}	NO
FRB20190224C	437.5	7.90	0.51	2.35×10^{41}	NO
FRB20190422A	372.8	9.10	0.44	1.96×10^{41}	NO
FRB20181218A	1727.2	1.59	2.02	9.10×10^{41}	NO
FRB20181219C	611.7	0.57	0.72	3.62×10^{40}	NO
FRB20181221A	291.8	5.80	0.34	7.12×10^{40}	NO
FRB20190519D	509.3	0.81	0.60	3.44×10^{40}	NO
FRB20190131D	574.6	6.80	0.67	3.68×10^{41}	NO
FRB20190213D	1112.3	2.20	1.30	5.02×10^{41}	NO
FRB20181025A	530.9	2.68	0.62	1.22×10^{41}	NO
FRB20181115A	941.6	1.92	1.10	3.06×10^{41}	NO
FRB20181226C	315.0	2.70	0.37	3.98×10^{40}	NO
FRB20190403B	238.4	23.80	0.28	1.92×10^{41}	NO
FRB20190322A	996.5	10.10	1.17	1.84×10^{42}	NO
FRB20181225B	241.0	7.50	0.28	6.04×10^{40}	NO
FRB20190630D	279.8	2.60	0.33	2.99×10^{40}	NO
FRB20181203A	589.2	3.60	0.69	2.08×10^{41}	NO
FRB20190221C	1821.7	7.10	2.13	4.53×10^{42}	NO
FRB20181223C	92.6	2.84	0.11	3.15×10^{39}	NO
FRB20190210C	588.1	3.60	0.69	2.08×10^{41}	NO
FRB20190416B	554.8	1.47	0.65	7.45×10^{40}	NO
FRB20190201B	695.0	2.30	0.81	1.89×10^{41}	NO
FRB20190625A	279.0	11.90	0.33	1.37×10^{41}	NO
FRB20190211A	1084.4	5.80	1.27	1.26×10^{42}	NO
FRB20190518G	461.9	1.76	0.54	5.94×10^{40}	NO
FRB20190519F	755.7	4.00	0.88	3.94×10^{41}	NO
FRB20190302A	813.5	35.00	0.95	4.07×10^{42}	NO
FRB20190410B	563.8	0.45	0.66	2.36×10^{40}	NO
FRB20190418A	114.4	2.20	0.13	3.46×10^{39}	NO
FRB20190107B	96.1	4.30	0.11	4.77×10^{39}	NO
FRB20190405B	1059.3	17.50	1.24	3.61×10^{42}	NO
FRB20190304B	447.4	2.22	0.52	6.90×10^{40}	NO
FRB20181014B	785.4	1.88	0.92	2.04×10^{41}	NO
FRB20181130A	125.0	1.27	0.15	2.70×10^{39}	NO
FRB20190131E	236.5	5.10	0.28	4.11×10^{40}	NO
FRB20190515A	293.1	16.80	0.34	2.06×10^{41}	NO
FRB20190604G	181.6	4.49	0.21	1.95×10^{40}	NO
FRB20180916A	217.6	4.50	0.25	2.84×10^{40}	NO
FRB20181030D	165.9	5.90	0.19	2.07×10^{40}	NO
FRB20190520A	352.8	2.40	0.41	4.43×10^{40}	NO
FRB20190304A	433.9	2.90	0.51	8.63×10^{40}	NO
FRB20190308C	477.4	4.80	0.56	1.75×10^{41}	NO
FRB20190319A	1932.3	19.40	2.26	1.39×10^{43}	NO
FRB20190102A	655.6	4.20	0.77	3.09×10^{41}	NO
FRB20190430C	301.5	5.10	0.35	6.66×10^{40}	NO
FRB20190102B	326.1	3.90	0.38	6.10×10^{40}	NO
FRB20190401A	740.8	8.60	0.87	8.25×10^{41}	NO
FRB20190219A	578.4	0.96	0.68	5.37×10^{40}	NO
FRB20181219B	1914.9	27.00	2.24	1.91×10^{43}	NO
FRB20190515B	789.7	11.30	0.92	1.22×10^{42}	NO
FRB20181229A	912.6	4.00	1.07	6.01×10^{41}	NO
FRB20190130B	959.3	2.95	1.12	4.89×10^{41}	NO
FRB20190403E	176.3	76.00	0.21	3.30×10^{41}	NO
FRB20190502C	349.4	8.30	0.41	1.53×10^{41}	NO
FRB20190423D	430.3	18.00	0.50	5.13×10^{41}	NO
FRB20190426A	284.8	2.01	0.33	2.31×10^{40}	NO

— *Continued from previous page*

TNS name	DM _E (pc cm ⁻³)	Fluence (Jy ms)	<i>z</i>	E (erg)	Repeat
FRB20190111B	1271.8	0.78	1.49	2.38×10 ⁴¹	NO
FRB20181226D	320.4	3.00	0.37	4.42×10 ⁴⁰	NO
FRB20181030E	109.8	6.30	0.13	9.92×10 ³⁹	NO
FRB20190404A	1313.6	4.50	1.54	1.47×10 ⁴²	NO
FRB20190501B	740.5	3.20	0.87	3.07×10 ⁴¹	NO
FRB20180922A	414.4	7.70	0.48	2.01×10 ⁴¹	NO
FRB20190419B	112.8	7.90	0.13	1.24×10 ⁴⁰	NO
FRB20181215B	453.4	2.90	0.53	9.39×10 ⁴⁰	NO
FRB20190318A	333.9	14.20	0.39	2.35×10 ⁴¹	NO
FRB20190517C	147.6	8.70	0.17	2.41×10 ⁴⁰	NO
FRB20190103C	1193.6	13.40	1.40	3.58×10 ⁴²	NO
FRB20190601C	237.7	5.80	0.28	4.67×10 ⁴⁰	NO
FRB20190427A	370.8	9.50	0.43	1.95×10 ⁴¹	NO
FRB20181116A	318.3	5.23	0.37	7.71×10 ⁴⁰	NO
FRB20190623B	1413.0	2.78	1.65	1.05×10 ⁴²	NO
FRB20181129A	299.2	3.10	0.35	4.05×10 ⁴⁰	NO
FRB20181214A	283.9	0.41	0.33	4.71×10 ³⁹	NO
FRB20190605C	149.8	4.40	0.18	1.38×10 ⁴⁰	NO
FRB20181013A	261.2	3.50	0.31	3.51×10 ⁴⁰	NO
FRB20181203B	318.7	4.50	0.37	6.64×10 ⁴⁰	NO
FRB20181221B	1333.1	3.30	1.56	1.11×10 ⁴²	NO
FRB20181119C	240.3	3.50	0.28	2.82×10 ⁴⁰	NO
FRB20181202A	629.2	13.70	0.74	9.23×10 ⁴¹	NO
FRB20181220A	83.6	3.00	0.10	2.73×10 ³⁹	NO
FRB20190112A	383.8	16.20	0.45	3.66×10 ⁴¹	NO
FRB20190204B	1419.4	4.40	1.66	1.68×10 ⁴²	NO
FRB20190420B	779.4	15.10	0.91	1.60×10 ⁴²	NO
FRB20181117C	1707.6	3.00	2.00	1.68×10 ⁴²	NO
FRB20181231A	1333.7	2.20	1.56	7.38×10 ⁴¹	NO
FRB20190519G	356.6	22.00	0.42	4.28×10 ⁴¹	NO
FRB20181124B	696.7	4.80	0.81	3.94×10 ⁴¹	NO
FRB20190212B	559.0	3.70	0.65	1.88×10 ⁴¹	NO
FRB20190224D	696.7	6.10	0.81	5.01×10 ⁴¹	NO
FRB20181214C	599.5	5.00	0.70	2.98×10 ⁴¹	NO
FRB20190110A	284.2	3.80	0.33	4.37×10 ⁴⁰	NO
FRB20190219B	1643.4	14.40	1.92	7.43×10 ⁴²	NO
FRB20190606B	222.4	17.40	0.26	1.19×10 ⁴¹	NO
FRB20190601B	745.9	13.00	0.87	1.25×10 ⁴²	NO
FRB20181018C	265.0	3.30	0.31	3.31×10 ⁴⁰	NO
FRB20190415B	567.6	22.30	0.66	1.17×10 ⁴²	NO
FRB20190228B	1043.9	66.00	1.22	1.32×10 ⁴³	NO
FRB20190121A	338.0	10.80	0.40	1.89×10 ⁴¹	NO
FRB20190203A	374.7	4.00	0.44	8.61×10 ⁴⁰	NO
FRB20190411C	194.8	9.30	0.23	4.91×10 ⁴⁰	NO
FRB20181224E	545.3	10.30	0.64	5.05×10 ⁴¹	NO
FRB20190320E	243.3	12.30	0.28	9.91×10 ⁴⁰	NO
FRB20190428A	942.4	7.40	1.10	1.18×10 ⁴²	NO
FRB20181231B	150.3	2.34	0.18	7.32×10 ³⁹	NO
FRB20190701D	877.4	8.60	1.03	1.19×10 ⁴²	NO
FRB20190518C	402.4	14.80	0.47	3.68×10 ⁴¹	NO
FRB20181018B	180.7	7.90	0.21	3.43×10 ⁴⁰	NO
FRB20181022D	494.2	6.20	0.58	2.45×10 ⁴¹	NO
FRB20190124F	217.2	6.40	0.25	4.04×10 ⁴⁰	NO
FRB20190625D	616.5	12.10	0.72	7.68×10 ⁴¹	NO
FRB20180910A	626.3	5.60	0.73	3.66×10 ⁴¹	NO
FRB20190228A	398.9	35.80	0.47	8.91×10 ⁴¹	NO
FRB20190423A	211.0	55.40	0.25	3.50×10 ⁴¹	NO

— Continued from previous page

TNS name	DM_E (pc cm^{-3})	Fluence (Jy ms)	z	E (erg)	Repeat
FRB20190624B	144.2	20.00	0.17	5.54×10^{40}	NO
FRB20190519H	1111.5	6.60	1.30	1.51×10^{42}	NO
FRB20180904A	305.7	6.00	0.36	8.34×10^{40}	NO
FRB20190106B	174.9	3.80	0.20	1.49×10^{40}	NO
FRB20190609B	239.9	22.20	0.28	1.79×10^{41}	NO
FRB20190412A	327.2	6.90	0.38	1.08×10^{41}	NO
FRB20190122C	665.5	47.00	0.78	3.55×10^{42}	NO
FRB20190210B	507.7	5.30	0.59	2.17×10^{41}	NO
FRB20190215B	138.4	5.60	0.16	1.36×10^{40}	NO
FRB20190330B	619.2	5.30	0.72	3.36×10^{41}	NO
FRB20190604C	351.7	26.20	0.41	4.83×10^{41}	NO
FRB20190224E	402.8	4.00	0.47	9.95×10^{40}	NO
FRB20181128D	113.8	7.00	0.13	1.10×10^{40}	NO
FRB20190118A	171.7	18.00	0.20	7.04×10^{40}	NO
FRB20190124C	282.2	13.70	0.33	1.58×10^{41}	NO
FRB20180923D	298.7	2.20	0.35	2.87×10^{40}	NO
FRB20190630B	501.6	14.70	0.59	6.03×10^{41}	NO
FRB20190527C	461.6	20.00	0.54	6.75×10^{41}	NO
FRB20181119B	166.8	94.00	0.20	3.68×10^{41}	NO
FRB20190627C	920.6	11.30	1.08	1.73×10^{42}	NO
FRB20181126A	444.6	9.40	0.52	2.92×10^{41}	NO
FRB20190417C	198.2	10.80	0.23	5.70×10^{40}	NO
FRB20190303B	146.4	42.00	0.17	1.16×10^{41}	NO
FRB20181226B	259.3	52.00	0.30	4.86×10^{41}	NO
FRB20190322C	1126.3	13.00	1.32	3.06×10^{42}	NO
FRB20190317F	1084.8	26.00	1.27	5.65×10^{42}	NO
FRB20190627B	388.3	10.20	0.45	2.31×10^{41}	NO
FRB20190323B	749.3	10.60	0.88	1.04×10^{42}	NO
FRB20190425A	79.4	31.60	0.09	2.31×10^{40}	NO
FRB20190614B	527.0	8.40	0.62	3.84×10^{41}	NO
FRB20190502B	884.8	10.10	1.03	1.40×10^{42}	NO
FRB20181104C	475.5	20.70	0.56	7.57×10^{41}	NO
FRB20190227A	330.6	12.50	0.39	2.07×10^{41}	NO
FRB20190111A	150.5	17.00	0.18	5.32×10^{40}	NO
FRB20181122B	171.4	22.00	0.20	8.61×10^{40}	NO
FRB20181224A	225.2	3.30	0.26	2.27×10^{40}	NO
FRB20190218C	275.6	31.00	0.32	3.33×10^{41}	NO
FRB20190502A	590.8	11.50	0.69	6.65×10^{41}	NO
FRB20190116C	587.4	65.00	0.69	3.76×10^{42}	NO
FRB20190421B	295.8	16.40	0.35	2.14×10^{41}	NO
FRB20190208B	653.6	14.30	0.76	1.02×10^{42}	NO
FRB20190607A	518.5	21.30	0.61	9.39×10^{41}	NO
FRB20190202A	266.6	95.00	0.31	9.54×10^{41}	NO
FRB20190404B	444.4	16.30	0.52	5.06×10^{41}	NO
FRB20181119A	330.3	3.50	0.39	5.79×10^{40}	YES
FRB20180908B	157.0	5.00	0.18	1.56×10^{40}	YES
FRB20181030A	62.3	8.20	0.07	3.57×10^{39}	YES
FRB20190209A	379.1	3.90	0.44	8.40×10^{40}	YES
FRB20190208A	508.4	4.90	0.59	2.01×10^{41}	YES
FRB20190421A	193.8	5.30	0.23	2.80×10^{40}	YES
FRB20181017A	1239.0	16.00	1.45	4.60×10^{42}	YES
FRB20190116B	423.7	2.00	0.50	5.70×10^{40}	YES
FRB20190417A	1301.9	5.80	1.52	1.84×10^{42}	YES
FRB20180916B	150.4	6.10	0.18	1.91×10^{40}	YES
FRB20181128A	338.0	8.10	0.40	1.42×10^{41}	YES
FRB20181119D	375.9	12.60	0.44	2.71×10^{41}	YES
FRB20190117A	345.2	9.90	0.40	1.73×10^{41}	YES

:

— *Continued from previous page*

TNS name	DM_E (pc cm^{-3})	Fluence (Jy ms)	z	E (erg)	Repeat
FRB20190222A	373.0	11.80	0.44	2.54×10^{41}	YES
FRB20190604A	520.9	7.80	0.61	3.44×10^{41}	YES

Notes. The first pulse of the repeating FRBs has been utilized in this work.